

2. Exoplanet microlensing

ANDREW GOULD

Microlensing is a powerful technique for detecting exoplanets because it is sensitive to low-mass planets beyond the snow line, free-floating planets, and planets in distant parts of the Milky Way and even other galaxies. These are all regions of parameter space that are very challenging (or impossible) for other techniques. However, microlensing planet detections are themselves very challenging. The observations require complex international cooperation, and the interpretation of events is mathematically sophisticated and at times near the limit of computational feasibility.

2.1. Introduction

Microlensing was first investigated by Einstein 100 years ago in unpublished notes (Renn, Sauer and Stachel 1997). He concluded that the phenomenon was so rare that it would never be observed, and indeed he only wrote it up in journal form (Einstein 1936) because he was harassed by the amateur scientist R. W. Mandel. Long before practical microlensing experiments were first proposed by Paczyński (1986), Liebes (1964) had already suggested that planets could be found. At about the same time, Refsdal (1964, 1966) pointed out the possibility of measuring ‘microlens parallaxes’ and using microlensing to measure the masses of isolated stars, two ideas that play a major role in planetary microlensing today, nearly 50 years later. However, practical microlensing-planet searches were triggered by the more recent work of Mao and Paczyński (1991) and Gould and Loeb (1992).

2.2. Microlensing basics

2.2.1 Point lenses

Planetary microlensing can usually be described as a short-lived perturbation on point-lens microlensing. Starting with the Einstein bending angle $\alpha = 4GM/(bc^2)$ and using the small-angle approximation, one immediately finds $(\theta_I - \theta_S)D_S = \alpha D_{LS}$, where M is the mass of the lens, b is the impact parameter, D_L , D_S and D_{LS} are the distances between the observer, lens and source, and θ_S and θ_I are the angular separations of the source and image, respectively, relative to the lens. This directly yields a quadratic equation that relates θ_I to θ_S through the so-called ‘angular Einstein radius’ θ_E :

$$(\theta_I - \theta_S)\theta_I = \theta_E^2 \equiv \kappa M \pi_{\text{rel}}; \quad \kappa \equiv \frac{4G}{c^2 \text{AU}} \simeq 8.1 \frac{\text{mas}}{M_\odot}. \quad (2.1)$$

Here $\pi_{\text{rel}} = \text{AU}/D_L - \text{AU}/D_S$ is the lens–source relative parallax. See Figure 2.1. This can be solved:

$$u_\pm = u \pm \sqrt{\frac{u^2 + 4}{2}}; \quad u \equiv \frac{\theta_S}{\theta_E}; \quad u_\pm \equiv \frac{\theta_{I\pm}}{\theta_E}. \quad (2.2)$$

Note that for stellar masses ($M \sim M_\odot$) and Galactic distances ($D_L \sim \text{kpc}$), θ_E is $\mathcal{O}(\text{mas})$ and so cannot be directly observed using current instruments. What can be observed is

Astrophysical Applications of Gravitational Lensing, ed. E. Mediavilla et al. Published by Cambridge University Press. © Cambridge University Press 2016.

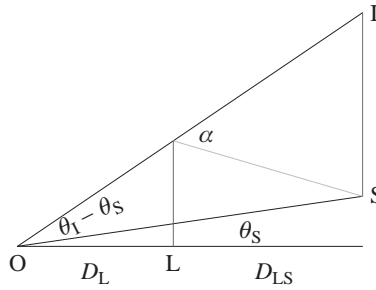


FIGURE 2.1. Point-lens geometry. Light from source (S) at distance $D_S = D_L + D_{LS}$ is deflected by lens (L) of mass M at distance D_L to observer (O), creating an image (I) at angle θ_I from lens, compared to θ_S for source. By the small-angle approximation, $\alpha D_{LS} = (\theta_I - \theta_S) D_S$. Making use of the Einstein bending angle $\alpha = 4GM/(c^2 \theta_I D_L)$, one obtains the quadratic equation $(\theta_I - \theta_S)\theta_I = \theta_E^2 \equiv \kappa M \pi_{\text{rel}}$ (see equation 2.1), which can then be solved to find the lensed image positions (equation 2.2).

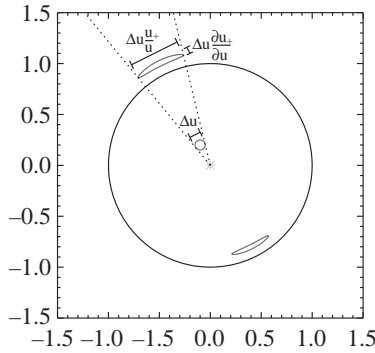


FIGURE 2.2. Geometry of point-lens/point-source magnification. Each image of the source is stretched in the transverse direction by a factor $\pm u_{\pm}/u$ and compressed in the radial direction by a factor $\partial u_{\pm}/\partial u$, which yields equation (2.3). (Figure courtesy of J. C. Yee.)

the magnification. If the lens does not pass directly over the source, then this is given by the determinant of the transformations from the source plane to the image plane for each image separately (see Figure 2.2):

$$A_{\pm} = \pm \frac{u_{\pm}}{u} \frac{\partial u_{\pm}}{\partial u} = \frac{A \pm 1}{2}; \quad A = A_+ + A_- = \frac{u^2 + 2}{u\sqrt{u^2 + 4}}. \quad (2.3)$$

Since the images cannot be resolved, one is normally only interested in the total magnification A . The limiting forms of this quantity are extremely important:

$$A(u) \rightarrow \frac{1}{u} \quad (u \ll 1); \quad A(u) \rightarrow 1 + \frac{2}{(u^2 + 2)^2} \quad (u \gg 1). \quad (2.4)$$

This means that the magnification rapidly becomes negligible outside the Einstein ring and has a very simple form well inside it. Hence, deviations from simple point-lens microlensing can usually be easily spotted. An important point-lens deviation occurs when the lens passes directly over the source. The profile then becomes more flat-topped owing to finite-source effects (Gould 1994). At the very centre, the magnification (ratio of image-to-source areas) becomes especially simple to evaluate. Since the source is a

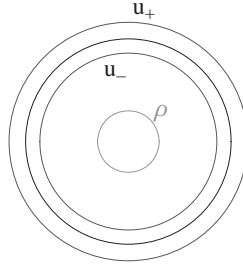


FIGURE 2.3. Magnification of perfectly aligned source of radius $\theta_* = \rho\theta_E$ is given by the ratio of the image area (annulus) to source area (circle), assuming no limb darkening. Hence $A = (1 + 4\rho^{-2})^{1/2}$, which goes to $2/\rho$ and $(1 + 2/\rho^2)$ in opposing limits. See equation (2.5).

circle and the image is an annulus, $A = (\rho_+^2 - \rho_-^2)/\rho^2$, i.e.

$$A(\rho) = \sqrt{1 + \frac{4}{\rho^2}} \rightarrow \frac{2}{\rho}; \quad \rho \equiv \frac{\theta_*}{\theta_E}, \quad (2.5)$$

where θ_* is the angular size of the source and the limit applies for $\rho \ll 1$. See Figure 2.3. Since main-sequence stars at several kpc have $\theta_* \sim \mathcal{O}(\mu\text{as})$, such transits usually occur only in very high-magnification events $A_{\text{max}} > 300$, but these are very important, as we will see.

The fact that sources are magnified does not in itself permit us to identify them as such because we do not necessarily know how bright they were before. But for Galactic microlensing, the magnification changes on an Einstein-radius crossing time t_E :

$$t_E = \frac{\theta_E}{\mu_{\text{rel}}}; \quad \mu_{\text{rel}} \equiv \mu_L - \mu_S, \quad (2.6)$$

where μ_{rel} is the lens–source relative proper motion. Since typical Galactic proper motions are a few mas/yr, t_E is typically a few weeks, although in extreme cases it can be several years or less than one day. Then, by the Pythagorean theorem, the observed flux varies with time as,

$$F(t) = A[u(t)]F_S + F_B; \quad u(t) = \sqrt{u_0^2 + \frac{(t - t_0)^2}{t_E^2}}, \quad (2.7)$$

where t_0 is the time of closest approach, u_0 is the value of u at this time, F_S is the source flux, and F_B is the blended flux (light in the photometric aperture but not participating in the event). Hence, five parameters are needed to describe most microlensing events (six, if ρ is needed). And if there is more than one observatory, then an additional two parameters ($F_{S,i}$, $F_{B,i}$) are needed for each observatory $i = 1 \dots n$. Note, from equations (2.1) and (2.6), that t_E is a complicated combination of M , π_{rel} and μ_{rel} , so one does not separately measure these quantities in most microlensing events.

However, for some special events, it is possible to measure the so-called microlens parallax vector, π_E , whose direction is the same as μ_{rel} and whose magnitude is $\pi_E = \text{AU}/\tilde{r}_E$, where \tilde{r}_E is the Einstein radius projected onto the observer plane. See Gould (2004) and Figure 2.4 for various pictorial representations of π_E . Usually, π_E is measured when the event is long enough that Earth’s orbit imprints distortions on the light curve (Gould 1992; Poindexter et al. 2005), but occasionally simultaneous observations from several observatories on Earth (Gould et al. 2009; Yee et al. 2010) or space (Dong et al. 2007) yield a measurement. If both π_E and θ_E are measured, then one can recover M

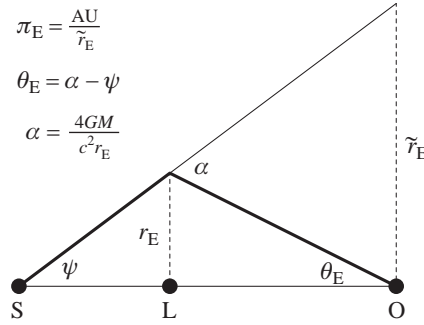


FIGURE 2.4. Geometric derivation of microlensing parameters π_E and θ_E . Light is bent by angle α by lens (L) of mass M on its way from source (S) to observer (O), creating a net angular displacement θ_E . This corresponds to a distance r_E on the lens plane, which is \tilde{r}_E projected on the observer plane. The three displayed equations are the definition of π_E , the exterior angle formula, and the Einstein bending angle. By the small angle approximation, $\theta_E \tilde{r}_E = \alpha r_E = 4GM/c^2$ and $\theta_E = \alpha - \psi = \tilde{r}_E(D_{OL}^{-1} - D_{OS}^{-1}) = \pi_{\text{rel}}/\pi_E$, where π_{rel} is the lens–source relative parallax. Together these yield: $\pi_{\text{rel}} = \theta_E \pi_E$, $M = \theta_E/(\kappa \pi_E)$, $\theta_E^2 = \kappa M \pi_{\text{rel}}$, $\pi_E^2 = \pi_{\text{rel}}/(\kappa M)$, where $\kappa \equiv 4G/(c^2 \text{AU})$. See equations (2.1) and (2.8). (Adapted from Gould 2000.)

and π_{rel} :

$$\pi_E = \sqrt{\frac{M}{\kappa \pi_{\text{rel}}}}; \quad M = \frac{\theta_E}{\kappa \pi_E}; \quad \pi_{\text{rel}} = \theta_E \pi_E. \quad (2.8)$$

In particular, since θ_* can be recovered from an instrumental colour–magnitude diagram of the event (Yoo et al. 2004), one can measure $\theta_E = \theta_*/\rho$ any time there are finite source effects. While in practice there are only two point-lens events (out of 20 000 total) with well-measured masses from microlensing data alone (Gould et al. 2009; Yee et al. 2010), the required higher-order parameters (θ_E and π_E) are actually much more easily obtained in binary-lens and planetary-lens events.

2.2.2 Binary lenses

Binary lenses are generalizations of point lenses in two distinct but related ways. From the standpoint of the lens equation, there is one additional point mass that is ‘tugging’ on the light. From the standpoint of event characterization, there are three additional parameters required to describe the event. The lens equation is generalized by

$$\mathbf{u} - \mathbf{y} = -\frac{\mathbf{y} - \mathbf{y}_L}{|\mathbf{y} - \mathbf{y}_L|^2} \rightarrow \mathbf{u} - \mathbf{y} = -\sum_{i=1}^n \epsilon_i \frac{\mathbf{y} - \mathbf{y}_{m,i}}{|\mathbf{y} - \mathbf{y}_{m,i}|^2}; \quad \epsilon_i \equiv \frac{m_i}{M_{\text{tot}}}. \quad (2.9)$$

Here \mathbf{u} and \mathbf{y} are the positions of the source and image relative to some arbitrary coordinate centre, and the $\mathbf{y}_{m,i}$ are the positions of the n masses ($n = 2$ for binary lenses). All quantities are normalized to the Einstein radius θ_E . In other words, the displacement of the source from the image ($‘u - y’$) is equal to the sum of the deflections due to each mass ($‘\epsilon_i/(y - y_{m,i})’$). We can see that the left-hand expression (equivalent to $n = 1$ of the right-hand one) is the same as the point-lens equation by setting $\mathbf{y}_L = 0$. Therefore, \mathbf{u} and \mathbf{y} must be parallel, so the equation can be written in scalar form as $(y - u)y = 1$, which is equivalent to $(\theta_I - \theta_S)\theta_I = \theta_E^2$, taking account of the fact that equation (2.9) is scaled to θ_E . As originally pointed out by Witt (1990), this equation is more easily solved

when written in complex form:

$$\zeta = z - \sum_i \frac{\epsilon_i}{\bar{z} - \bar{z}_{m,i}}; \quad \zeta \equiv u_1 + iu_2, \quad z \equiv y_1 + iy_2. \quad (2.10)$$

This equation can be transformed into a fifth-order polynomial (tenth-order for a triple lens). Such an equation must be solved numerically. See for example Skowron & Gould (2012) and references therein. However, the magnifications so derived are only valid when the magnification changes slowly across the face of the source. The real difficulty occurs when this assumption fails, i.e. when the source is close to or transiting a caustic. I will review numerical methods for finding solutions below.

From the standpoint of event characterization, three additional parameters are needed: (s, q, α) . s specifies the separation of the binary components in units of θ_E . The mass ratio is $q = \epsilon_2/\epsilon_1$. And α is the angle of the source trajectory relative to the binary axis. In strong contrast to the point-lens case, one must almost always specify ρ because binary events are typically recognized because the source passes over or very close to a caustic. This means that $\theta_E = \theta_*/\rho$ is almost always measured. From equation (2.1), this means that the product $M\pi_{\text{rel}}$ is known. In addition, since t_E is routinely measured, it means that the relative proper motion $\mu_{\text{rel}} = \theta_E/t_E$ is also measured.

Binary-lens caustics come in three topologies: close, wide, and intermediate. Intermediate binaries ($s \sim 1$) have a single caustic with six concave sides. As s moves towards lower values ('close binaries'), this 'resonant' caustic breaks up into three simpler caustics, including one four-sided 'central' caustic and two (symmetric about the lens-axis) triangular caustics. As the mass ratio decreases towards planetary values, these two caustics move together towards the lens axis, creating a narrow trough of demagnification between them. These two caustics are called 'close planetary caustics' in this regime. The physical reason for these caustics is that the image is passing close to the position of the planet. From the point-lens equation, then, the source-plane position u of the caustic is related to the position of the image (and so planet), by $s^{-1} - s = u$, or $-s = u_- = (u - (u^2 + 4)^{1/2})/2$. The physical meaning of the 'negative' u_- position is that the close planetary caustics are on the opposite side of the host star from the planet. That is, the planet is perturbing the 'minor image' (interior to the Einstein ring) because of the host.

On the other hand, as the binary separates towards wider values, the resonant caustic breaks up into two four-sided caustics, each associated with one of the masses. In the planetary-mass regime, the caustic associated with the host is smaller than the one associated with the planet by roughly $q^{1/2}$. That is, the planetary caustic is smaller than the Einstein radius by about $q^{1/2}$, and the host (or 'central') caustic is yet smaller by another factor of $q^{1/2}$. As in the close-binary case, the position of this caustic is given by the point-lens equation: $s - s^{-1} = u$ or $s = u_+ = (u + (u^2 + 4)^{1/2})/2$. Han (2006) has an excellent guide to the sizes and positions of planetary caustics, by which one can essentially solve all planetary-caustic microlensing events without a computer. I will give an example further below.

As with single-lens events, binary lenses can be fit for parallax π_E . However, the frequency of precision measurements is substantially higher than for point lenses because the added structure of the caustics helps 'pin down' the light curve (An & Gould 2001).

In addition, binary-lens events often yield orbital-motion information on the binary. This is more surprising because the orbital periods are typically several years, while the binary-induced perturbations usually last only a few days. Thus, the first such measurement (Albrow et al. 2000) was initially believed to be a fluke due to special geometry. And this event only yielded the two components of orbital motion in the plane of the

sky: $\gamma_{\parallel} = (ds/dt)/s$ the fractional time rate of change of s , and γ_{\perp} the instantaneous angular velocity of the binary. However, over time, binary motion has been measured in a very large number of events. Quite incredibly, there are now three events with complete orbital solutions (Shin et al. 2011, 2012). In microlensing terms, these solutions require the parameters: $F_S, F_B, t_0, u_0, t_E, \rho, s, q, \alpha, \pi_E, s_z, \gamma_{\parallel}, \gamma_{\perp}, \gamma_z$, where s_z and γ_z are the instantaneous position and velocity of the companion out of the plane of the sky. The relation between these parameters and the eight standard Kepler parameters (two masses, five Kepler invariants, phase) is described in detail by Skowron et al. (2011). The lens in one of these events (OGLE-2011-BLG-0417) is bright enough to permit radial-velocity measurements, which could test the microlens solution (Gould et al. 2013).

2.3. Solving the lens equation

Gould and Loeb (1992) argued that planetary-caustic microlensing events could be basically solved by simple inspection, and this is actually true of many of them, most dramatically OGLE-2005-BLG-169 (Beaulieu et al. 2006) and MOA-2009-BLG-266 (Muraki et al. 2011). However, it is actually rare that central-caustic events can be understood by inspection. Moreover, measurement of higher-order effects certainly requires detailed modelling. There are several complementary approaches to such modelling.

By taking the complex conjugate of the lens equation (2.10) $\bar{z} = \bar{\zeta} + \sum_i \epsilon_i / (z - z_i)$ and then substituting back into it, one obtains

$$(z - \zeta) \prod_{i=1}^2 (\bar{\zeta} + Q - \bar{z}_i) = \sum_{i=1}^2 (\bar{\zeta} + Q - \bar{z}_i) \epsilon_{3-i}; \quad Q \equiv \sum_{i=1,2} \frac{\epsilon_i}{z - z_i}. \quad (2.11)$$

Multiplying this equation by $[(z - z_1)(z - z_2)]^2$ then yields a fifth-order polynomial in z , which can be solved using Laguerre's method, or somewhat more sophisticated techniques (Skowron & Gould 2012). There will of course be five formal solutions, but two of these may not solve the original lens equation. Thus, there will be three or five genuine solutions. From these one can evaluate the magnifications:

$$A = \sum_i |A_i|; \quad A_i = \frac{1}{1 - |\partial\zeta_i|^2}; \quad \partial\zeta_i = \sum_k \frac{\epsilon_k}{(\bar{z} - \bar{z}_k)^2}. \quad (2.12)$$

If the magnification is roughly constant over the face of the source, or even if it varies linearly, this approach will be fine. For somewhat non-linear variations, one can employ the quadrupole or hexadecapole approximations (Pejcha & Heyrovský 2009), for which Gould (2008) gives a detailed prescription that takes rigorous account of limb darkening of the source. These require 5 or 13 calls to the 'lens solver' (a subroutine that solves the lens equation for a point source), which is still extremely cheap compared to the methods described below.

Conceptually, the simplest approach is inverse ray-shooting. That is, one uniformly samples the image plane (\mathbf{y} in equation 2.9) with rays that are traced back to the source plane (\mathbf{u}). Then, for each source position, one finds all the rays that landed within the source and counts them up (weighted by the source surface brightness). This method is completely immune to the presence of caustics because the grid of rays is uniform on the image plane, not the source plane where the caustics reside. The major downsides are that it is computationally intensive, and that one must take measures to ensure that all of the images are actually covered. There are two ways of handling these challenges, each with its own difficulties. In one approach (Bennett et al. 2010), one shoots rays starting at a position of each image (found from equation 2.11) and extends these until

the boundary of the source is covered. In another (Dong et al. 2006), one shoots a large fraction of the image plane (chosen so that these map onto the source plane to cover all caustics that the source might pass over) and then makes a pixelated density map in the source plane. Source magnifications are then calculated from individual pixels that lie within the source and from individual rays that make up boundary pixels. The first method is computationally more intensive, but allows for changing values of s as the event evolves. The second method permits one to rapidly find the best-fit model for a given (s, q) ‘map’, but does not permit s to change during an event.

An alternate approach is contour integration (Gould & Gaucheron 1997). Here one maps the boundary of the source onto the image plane, using equation (2.11), and evaluates the areas of the images using Stokes’s theorem. The magnification is simply this area divided by the area of the source. By eliminating one dimension of integration, this method is much faster than inverse ray-shooting. It also permits changing s . In the form just described, it does not allow for limb darkening of the source, but this can be well approximated (at some computational cost) by evaluating a series of source annuli with different surface brightnesses. A more efficient version of this algorithm is described by Bozza (2010).

2.4. Fitting light curves

There are two distinct problems in fitting light curves: finding a good fit to the data and determining whether this fit is unique. There has been substantial progress in developing a systematic approach to both, but in the most difficult cases both remain something of an art.

2.4.1 Fitting by eye

There are many cases in which the basic solution can be derived by eye. A good example is MOA-2009-BLG-266 (Muraki et al. 2011). See Figure 2.5. The source is extremely bright and so unlikely to be significantly blended (which can be checked later). If one simply ignores the small planetary perturbation a few days before peak, the event looks like a simple point lens, from which one can directly estimate $t_0 = 5093.1$ and $A_{\max} = 7.6$, and so, using the limiting form $u = A^{-1}$, estimate $u_0 = 0.132$. Then one can estimate t_E either by directly finding the times when the light curve falls to $A = A(u = 1) = (9/5)^{1/2} \simeq 1.34$ or from the formula (valid for relatively high-magnification events) for the full width half maximum $t_{1/2} = 12^{1/2} u_0 t_E$. Either way, one finds $t_E = 60$ days.

We then move on to find the planetary parameters. First, by inspection, the planetary perturbation is centred at $t_{0,\text{planet}} = 5086.5$, which is offset from the peak by $\tau_{\text{planet}} = (t_0 - t_{0,\text{planet}})/t_E = 0.11$. One can then estimate the normalized source–lens separation u_{planet} at the time of the planetary perturbation in two ways. First, by inspecting the magnification at this time (interpolating over the perturbation), from which one derives $u_{\text{planet},1} = A_{\text{planet}}^{-1} = 0.154$. Second, by $u_{\text{planet},2} = (u_0^2 + \tau_{\text{planet}}^2)^{1/2} = 0.172$. We take the average $u_{\text{planet}} = 0.163$.

Next, we note that the planetary perturbation is a sharp negative dip, by about 0.6 mag. This means that the planet has largely destroyed one of the two images, which are in the ratio $A_+/A_- = (A + 1)/(A - 1) \sim (1 + u)/(1 - u) = 1.4$. If the minor image had been completely destroyed, then the dip would be $2.5 \log(2.4/1.4) = 0.6$. Unlike major images, minor images are easily destroyed because they form from saddle points on the time-delay surface. As mentioned above, planets with $s < 1$ perturb the minor image, and have large negative deviations right on the planet–star axis. We therefore evaluate

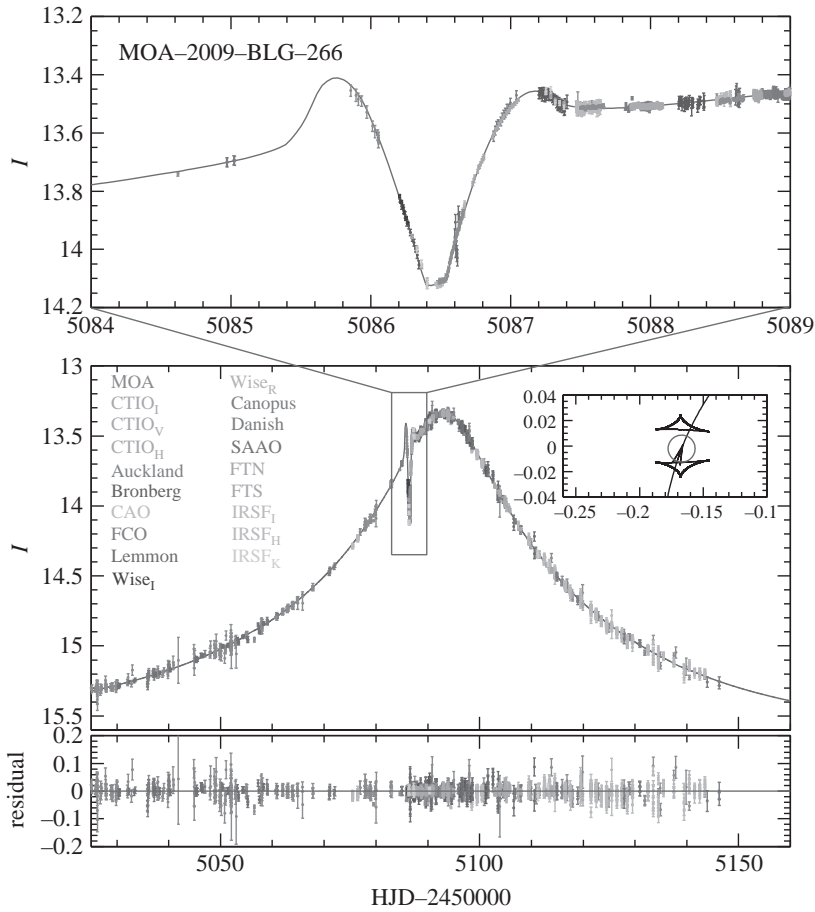


FIGURE 2.5. Light curve of MOA-2009-BLG-266, with zoom of planetary perturbation (top panel) and residuals (bottom panel). As described in detail in Section 2.4.1, it is possible to estimate the main microlensing parameters (t_0 , u_0 , t_E , q , s , α , ρ) very accurately by eye. See Table 2.1 for a summary of the ‘by eye’ and ‘computer’ results. (Figure courtesy of C. Han.)

(equation 2.2)

$$s = \frac{-u_{\text{planet}} + (u_{\text{planet}}^2 + 4)^{1/2}}{2} = 0.922. \quad (2.13)$$

Simple geometry yields $\sin \alpha = u_0/u_{\text{planet}}$. Hence $\alpha = 54^\circ$.

We still must evaluate the mass ratio q and the normalized source size ρ . First ρ . The planetary perturbation is composed of two slanting ‘walls’ whose functional form reminds us of the generic fold caustic crossings (exit then entrance) shown in Gould and Andronov (1999), from which we see that from peak to break-point (complete exit) is 1.7 times the source crossing time t_{cross} . By eye, these duration are 0.69 days and 0.65 days respectively. Taking the average and dividing by 1.7 yields $t_{\text{cross}} = 0.397$ days. The caustic walls are parallel to the planet–star axis. Hence, the source self-crossing time is $t_* = t_{\text{cross}} \sin \alpha = 0.32$ day. Thus $\rho = t_*/t_E = 5.3 \times 10^{-3}$.

Finally, by noting that the short ‘flat trough’ between the two sloping walls lasts just $t_{\text{flat}} = 0.15$ days, we can reconstruct the interval between the times when the centre of the source passed each caustic wall, $\Delta t = 2t_{\text{cross}} + t_{\text{flat}} = 0.95$ days. Taking account of

TABLE 2.1. MB09266: eye vs. computer

Parameter	Eye	Computer
t_0	5093.1	5093.26
u_0	0.13	0.131
t_E	60 d	61.6 d
q	5.8×10^{-5}	5.4×10^{-5}
s	0.922	0.914
α	54°	50°
ρ	5.3×10^{-3}	5.2×10^{-3}

the angle α of the trajectory, this corresponds to a separation between the caustic ‘walls’ of $\Delta u = (\Delta t/t_E) \sin \alpha = 0.0128$. According to Han (2006),

$$\Delta u = 4\sqrt{\frac{q u_{\text{planet}}}{s}} \Rightarrow q = \frac{s}{u_{\text{planet}}} \left(\frac{\Delta u}{4} \right)^2 = 5.8 \times 10^{-5}. \quad (2.14)$$

It is of some interest to compare these results, which were obtained by staring at the light curve on a computer screen, with the published best fit model. See Table 2.1.

However, even this event has a measurable higher-order effect, microlens parallax, whose measurement then yielded the lens mass and distance, which are very important. In this case, one can simply start with the by-eye model and perturb it via, for example, a Monte Carlo Markov chain (MCMC) to find the best fit including π_E .

2.4.2 Blind searches

However, in some cases, the basic solution is by no means obvious. This can happen for several reasons. Probably the most difficult case is that of high-magnification events. In these, the perturbation is due to the small (‘central’) caustic near the host star, rather than the larger (‘planetary’) caustic directly associated with the planet. Because the central caustic is smaller, there are intrinsically many fewer central-caustic events. However, *given* that there is a high-mag event, the probability of a planet detection is much higher than for more typical low-mag events. And high-mag peaks can be predicted in advance from the rising light curve. Hence, many planets have been detected through this channel.

The main problem with analysing high-mag events can be seen from direct comparison with MOA-2009-BLG-266 (Section 2.4.1). There we could immediately read off the point-lens parameters (t_0, u_0, t_E) from the unperturbed portion of the light curve. This is not quite as easy with a high-mag event but still usually basically possible. More critical, for MOA-2009-BLG-266, we could directly infer s and α from the time of the planetary perturbation, whereas this moment is, in a high-mag event, by definition $\sim t_0$, and so contains almost no information. While one can learn some tricks to guess the parameters of some high-mag events, even in these cases it is difficult to determine whether these are unique solutions. Hence, comprehensive blind searches are required.

There are basically two approaches that have been developed, each closely related to the modelling techniques discussed in Section 2.3. One method is to form a grid of (s, q) χ^2 ‘maps’, using a set of MCMCs. Each MCMC begins with a common set of four parameters (t_0, u_0, t_E, ρ) that can be robustly estimated from the light curve. The first three can be guessed from the overall morphology of the light curve while the fourth can usually be estimated from the caustic-crossing time of some caustic feature. Since α

typically cannot be guessed, a grid of initial trial values is chosen around the unit circle. In the second method, one chooses several dozen seeds that are representative of various light curve topologies and then allows all parameters to vary. Most often, both methods work and the identified solutions are similar. However, from time to time, one method misses a solution identified by the other, which leads to further fine-tuning of methods.

After one (or several) basic solutions are found, each can be further investigated by including more higher-order parameters and/or denser search grids.

2.4.3 Degeneracies

Of course, the biggest worry is that solutions that are equally good or better than the best identified one have been missed. In this regard, it is important to recognize that there are three degeneracies that are buried deep in the lens equation itself. Hence, these degenerate solutions should always be checked once a solution is identified.

The first of these is the close-wide $s \leftrightarrow s^{-1}$ degeneracy, which was first discovered by Griest and Safizadeh (1998) when they pointed out the excellent planet-sensitivity of high-magnification events. Dominik (1999) found that this degeneracy applied to a wide range of binaries, not just the special case of high-mag events, and showed that it was rooted in a deep symmetry between the shear (wide) and quadrupole (close) limits of the lens equation. Finally, An (2005) analysed this symmetry at a still deeper level and found specific correspondences between (s, q) pairs in the wide and close limits. Note that the further s is from unity, the more difficult it is to break this degeneracy. This degeneracy applies only to central caustics, not planetary caustics. All central-caustic solutions must be tested for this degeneracy.

A second degeneracy was discovered in the context of microlensing parallax by Smith, Mao and Paczyński (2003) and was developed through several stages. In its most comprehensive form (Skowron et al. 2011),

$$(u_0, \pi_{E,\perp}, \alpha, \gamma_\perp) \leftrightarrow -(u_0, \pi_{E,\perp}, \alpha, \gamma_\perp). \quad (2.15)$$

Here, $\pi_{E,\perp}$ is the component of π_E perpendicular to the projected position of the Sun at the peak of the event. See Gould (2004) and Park et al. (2004). It has been dubbed the ‘ecliptic degeneracy’ because it is exact if the source lies on the ecliptic. Hence, if the source lies ‘near’ the ecliptic (and the whole Galactic bulge fits this definition in some sense) it can be very strong. Note that if $\pi_{E,\perp}$ is not measured, the degeneracy for the remaining parameters is exact. It is then of no interest and so is never reported in practice.

As with the $s \leftrightarrow s^{-1}$ degeneracy, the ecliptic degeneracy is discrete. But there is also a closely related continuous degeneracy between $\pi_{E,\perp}$ and γ_\perp , which was first noted by Batista et al. (2011) and further studied by Skowron et al. (2011). The importance of this degeneracy cannot be overstated. It means that if one fits *either* for $\pi_{E,\perp}$ or γ_\perp , one *must* fit for the other. Otherwise the central value of the fit parameter will be misestimated and its uncertainty underestimated due to effectively enforcing ‘zero’ on the unfit but correlated other parameter.

A third degeneracy is between parallax and ‘xallarap’, which refers to distortions in the light curve due to the orbit of the source around an unseen companion. Xallarap is a potentially nasty problem because *any* parallax signal due to the Earth’s orbit can in principle be mimicked by the action of a companion to the source. There are two strategies to vet against xallarap (or potentially, detect it).

To understand these, let us consider the simpler problem of trigonometric parallax. In general, it is said that astrometric parallax measurements return five ‘standard’

parameters: parallax π , plus two 2-dimensional vectors, proper motion $\boldsymbol{\mu}$ and instantaneous position $\boldsymbol{\theta}$. In fact, such measurements could return 11 parameters: these five plus the six Kepler parameters of the Earth's orbit projected on the sky. In fact, astrometrists generally do not fit for these extra six parameters because they consider the cause of the star's parallactic motion to be known: the Earth's motion. But, in principle, they could fit for these parameters and ask whether they were consistent with the Earth's motion. If yes, they would then impose the Earth's orbit as a further constraint. If no, this would be evidence that the parallax signal was in fact due to source motion (xallarap).

Let us now turn to microlens parallax, for simplicity focusing on point lenses. We are sensitive to source–lens separations relative to θ_E (rather than angles on the sky). Therefore, we can in principle measure 10 parameters. These are each analogous to the 11 parameters from trigonometric parallax except that we cannot measure both the direction of lens–source relative proper motion and the orientation of the Earth's reflex motion in the Einstein ring, only the relative angle between these two directions. That is, in place of $\boldsymbol{\theta}$ at some arbitrary time t , we have (τ, u_0) where $\tau = (t - t_0)/t_E$. Of course, in practice one reports t_0 rather than τ , but the two are equivalent. In place of $\boldsymbol{\mu}$ we have t_E^{-1} ; in place of π we have π_E ; and we (in principle) recover the same Kepler Earth parameters (scaled to the Einstein radius rather than an AU). Hence, when we impose the known orbit of Earth, we recover two parameters $\boldsymbol{\pi}_E$, i.e. both the amplitude of parallax π_E and the direction of proper motion.

Now, while in principle we could fit for all 10 parameters, in practice this is not possible because the events last only a small fraction of a year. Nevertheless, we can consider a reduced parameter space: three parameter circular orbits that are described by their period and orientation in space. If periods different from one year are significantly favoured, then this would be evidence for xallarap. Similarly, if one restricts to periods of one year and the favoured orbit orientation is significantly different from that of the Earth's orbit projected on the target, this would also be evidence. On the other hand, if the best fit is consistent with a one-year period, and most orientations other than the target's are excluded with high significance, this dramatically reduces the prior probability that the source would have a companion whose orbital characteristics exactly mimicked the Earth's.

Finally, while every parallax signal can be mimicked by *some* companion, not all of these companions are physical. For example, the mass of the companion might be inferred to be $10 M_\odot$. The fact that this companion is not seen would then require that it be a black hole. Such a companion would also be a priori highly improbable.

2.5. Microlensing parameter space

To date, microlensing planet searches have found only about 30 planets, i.e. 1–2 orders of magnitude fewer than transit and Doppler (RV) searches. However, microlensing probes very different regions of parameter space and hence even these few detections have yielded many important discoveries and surprises (Figure 2.6).

2.5.1 Planets beyond the snow line

By a seeming coincidence of Galactic geometry, microlensing is sensitive primarily to planets that are one-to-few times the snow line from their hosts. This is the region of the protoplanetary disc where ices first form, which greatly increases the solid materials available for protoplanet formation. In the Solar System, the snow line $a_{\text{snow},\odot} = 2.7 \text{ AU}$ is precisely measured. While the scaling to other stars is debated, it is generally thought to go as $a_{\text{snow}} = a_{\text{snow},\odot} (M/M_\odot)^\beta$ where $\beta \sim 1$. By comparison, the Einstein radius r_E ,

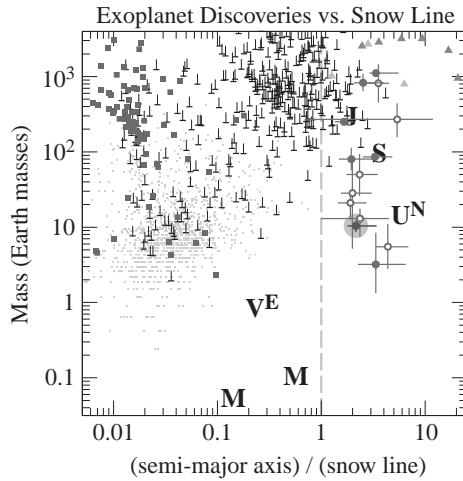


FIGURE 2.6. Planet discoveries as a function of semi-major axis and mass. Note that the semi-major axis is scaled to the assumed ‘snow line’ $a_{\text{snow}} = 2.7 M/M_{\odot}$. Shapes indicate detection method: microlensing (\diamond), RV (\circ), transits (\blacksquare), *Kepler* transit candidates (\blacksquare), imaging (\blacktriangle), timing (\triangle), Solar System (black letters). Open microlensing points have Bayesian mass estimates. Microlensing probes a region of parameter space that is virtually untouched by other methods. (From Muraki et al. 2011, *ApJ*, **741**, 22.)

which is the projected separation at which microlensing sensitivity to planets peaks is

$$r_E = D_L \theta_E = \left(\frac{4GM D_L D_{LS}}{c^2 D_S} \right)^{1/2} = 4 \text{ AU} \left(\frac{M}{M_{\odot}} \right)^{1/2} \left(\frac{D_L D_{LS}/D_S}{4 \text{ kpc}} \right)^{1/2}. \quad (2.16)$$

Hence, if in fact $\beta = 1$, then $r_E/a_{\text{snow}} = 1.5$ for $M = M_{\odot}$ solar-type hosts and $r_E/a_{\text{snow}} = 3$ for $M = 0.25 M_{\odot}$ mid- M -dwarf hosts. The true planet–host separation will be, on average, $(3/2)^{1/2} \sim 1.2$ times larger.

By contrast, RV sensitivity drops off at large distances owing to declining reflex velocity at fixed mass (and finite duration of the experiments) while current and presently conceivable transit experiments have no sensitivity at all in this region.

Since the nearby Universe contains about four times more mass in oxygen than the materials needed for rock (silicon, magnesium, iron), one might think that the ice/rock ratio in these regions would be 4:1. In fact, Ganymede, Callisto, and Titan, which are reasonable proxies for proto-solar solids beyond the snow line, all have ratios 1:1. Probably ice formation is fundamentally limited by silicate dust surface area, which provides a home for ice mantles. In any case, in the Solar System giant planet formation was seeded by rock–ice cores beyond the snow line, and hence this region is generally thought to be the nursery for giant planets around other stars. Thus microlensing enables probes of this critical region.

2.5.2 Mass not light

With the exception of microlensing, all planet-search techniques rely on light from the host (or in some cases, the planet itself). Microlensing does not make use of either: the light observed is from a more distant, unrelated star. Microlensing is sensitive only to the masses of the host and planet (and their projected separation). This means that microlensing is about equally sensitive *per star* to planets around all host stars, from

brown dwarfs to F and G stars. The only real exception is early-type stars: for main-sequence stars $M > 2 M_{\odot}$, the light from the host actually starts to interfere with observations of the source star by diluting its light. Microlensing is also sensitive to planets without hosts, so-called free-floating planets. It is impossible for methods that rely on host light, such as RV and transits, to detect free-floating planets, simply because they have no host. Such planets can be detected by direct imaging, but only if they are self-luminous, which basically applies only to young giant planets.

2.5.3 Distant planets

Microlensing naturally detects planets that are anywhere along the line of sight to the source star. Present surveys are focused on the Galactic bulge, which is 8 kpc away. Hence microlensing is uniquely able to probe planets at a range of positions in the Galaxy. Moreover, if microlensing surveys were carried out towards other galaxies, planets could be detected in these as well. There is no other method, nor even an idea for a method, to detect such extragalactic planets.

2.6. Microlensing results

Since the first microlensing planet, OGLE-2003-BLG-235Lb, was found a decade ago (Bond et al. 2004), microlensing planet detections have supplied a steady stream of surprises.

2.6.1 Super-jupiters orbiting M-dwarfs

OGLE-2005-BLG-071Lb, the second microlensing planet, had an exceptionally large mass ratio, $q = 7 \times 10^{-3}$ (Udalski et al. 2005). Since the host mass was not immediately known, it was not clear at the time whether this was surprising or not. However, Dong et al. (2009) subsequently showed, based on a variety of follow-up data combined with microlens parallax from the light curve, that the host is an M-dwarf, $M \sim 0.4 M_{\odot}$. This means that the planet is a super-jupiter, $m_p \sim 3 M_{\text{Jup}}$. Such planets are not supposed to form around M-dwarfs in the standard core-accretion paradigm (Laughlin, Bodenheimer and Adams 2004; Ida & Lin 2005), although they would form in the competing model of disc instabilities (Boss 2006).

While one such planet could be a statistical fluke, Batista et al. (2011) found a second super-jupiter orbiting an M-dwarf, MOA-2009-BLG-387Lb. In this case, the mass ratio was even higher, $q = 0.013$, while the host mass was probably somewhat lower (best fit $M = 0.19 M_{\odot}$, 90% confidence $0.07 < M/M_{\odot} < 0.49$). Future observations should determine whether M-dwarf/super-jupiter pairs are common.

2.6.2 Cold neptunes

The third and fourth microlensing planets, OGLE-2005-BLG-390Lb and OGLE-2005-BLG-169Lb, were both ‘cold neptunes’, i.e. Neptune-mass planets beyond the snow line (Beaulieu et al. 2006; Gould et al. 2006). The title of the second paper already claimed that ‘Cool Neptune-Like Planets Are Common’, and indeed this has been confirmed by two additional cold neptunes: OGLE-2007-BLG-368Lb (Sumi et al. 2010), and MOA-2009-BLG-266Lb (Muraki et al. 2011). All four of these planets have $q = 6\text{--}9 \times 10^{-5}$. To date, microlensing is the only technique that has detected cold neptunes, owing to its sensitivity to low-mass planets beyond the snow line. However, RV and transits are detecting large numbers of neptunes well within the snow line. It is still not clear whether

these form in situ, or migrate from beyond the snow line where the microlensing neptunes lie.

2.6.3 *Solar-like systems*

Stripped of non-essentials (like the Earth), the Solar System consists of three bodies: the Sun and two gas-giant planets beyond the snow line (Jupiter and Saturn). Are systems like this common? Microlensing is the only method that is currently sensitive to such systems and finds that the answer is ‘yes’.

The fifth and sixth microlensing planets were such a two-planet system, OGLE-2006-BLG-109Lb,c (Gaudi et al. 2008; Bennett et al. 2010). This system has very similar planet–star mass ratios and a very similar semi-major axis ratio to the Sun/Jupiter/Saturn system. The only real difference is that the host mass is half that of the Sun, and corresponding to this (and also to the idea that snow line scales linearly with mass) the semi-major axes are half as big as well. The discovery of a single such system already suggested that they may be common.

However, Han et al. (2013) recently discovered a second such system, OGLE-2012-BLG-0026Lb,c. In this case, the host is $M = 0.8 M_{\odot}$ and the mass ratios of the planets are $q = 7.8 \times 10^{-4}$ and 1.3×10^{-4} . These correspond to 80% of Jupiter’s mass ratio and 45% of Saturn’s mass ratio respectively. Both planets are projected near the Einstein ring, which enhanced their detectability but makes it impossible to reconstruct their physical separations. However, both are definitely beyond the snow line, even in projection. Thus, this system, while not a doppelganger for the Solar System (like OGLE-2006-BLG-109Lb,c), is qualitatively similar.

Although no rigorous statistical investigation has been made, the fact that there are two such detections among the first 15 published planets strongly suggests that they are common.

2.6.4 *Free-floating planets*

Microlensing is the only way to detect isolated dark objects, such as black holes and old isolated brown dwarfs or planets. Sumi et al. (2011) examined the time scale distribution of events detected by the MOA collaboration. This distribution has a ‘bump’ or excess at short duration, centred at $t_E \sim 1$ day. It is important to point out that it is actually impossible to get such a short-duration bump from an underlying distribution of stars and brown dwarfs that is smoothly distributed in mass and distance. Mao and Paczyński (1996) showed that such populations produce power-law tails in the time-scale distribution of $d\Gamma/d\ln t_E \propto t_E^{\pm 3}$, respectively. Hence, the only possible causes of this bump are (1) a discrete population of ‘free-floating planets’, (2) statistical noise, (3) other forms of stellar variability masquerading as microlensing. Examination of the individual events in the Sumi et al. (2011) sample shows that two of the shortest (so extremely unlikely to be statistical fluctuations in the underlying stellar population) are almost certainly microlensing. One, in particular, is a high-magnification event with a symmetric light curve.

Sumi et al. (2011) find that the most likely mass scale is $M \sim M_{\text{Jup}}$, which also follows naively from the 1-day typical time scale of these events. They also find that, at this mass scale, there would have to be two free-floating planets per star in the Galaxy. This does not mean ‘per G star’, but ‘per star’. It is very difficult to imagine how such a large population of free-floating planets could have been created, given that it is substantially larger than the number of Jupiter-mass planets that are bound to stars (as determined by either microlensing or RV). Nevertheless, it is also difficult to see what could have generated these short events except a new population. It should be pointed out that, if

these planets were at ten or more Einstein radii from their hosts, the planets would have been discovered without a trace of the host in the microlensing events. However, this does not solve the puzzle: it is no easier to see how to create such a huge population of distant planets. Fortunately, there are substantial additional data from both the OGLE and MOA collaborations that will permit further investigation.

2.6.5 Planet frequencies

In general it is quite difficult to specify the selection function for microlensing planets because of the haphazard, indeed chaotic, manner in which they are detected. However, Gould et al. (2010) argued that the high-magnification ($A_{\text{max}} > 200$) sample of the Microlensing Follow Up Network (μFUN) does constitute a statistical sample. This is because, however frantic and chaotic are μFUN 's calls to monitor these fast-paced events, the monitoring itself takes place independently of whether planets are being detected. They found a fairly high rate,

$$\frac{d^2 N_{\text{pl}}}{d \log q d \log s} = (0.36 \pm 0.15) \text{ dex}^{-2}, \quad (2.17)$$

centred at a Saturn-like mass ratio $q = 5 \times 10^{-4}$. This was the first such frequency measurement beyond the snow line. It is about five times higher than the rate found by Cumming et al. (2008) at separations ~ 30 times closer using the RV technique, when adjusted for different host masses and scaled to the snow line. If the close-in gas giants indeed arrive at their present locations by migration, this implies that most planets do not migrate, or at least do not migrate very far.

Gould et al. (2010) were not able to measure a slope in mass ratio. However, Cassan et al. (2012) combined these results with the slope estimate from Sumi et al. (2010) $dN/d \log q \propto q^{-0.68 \pm 0.20}$ and with their own independent search for microlensing planets using PLANET collaboration data. They concluded that $17^{+6}_{-9}\%$ of stars host jupiters, $52^{+22}_{-29}\%$ of stars host neptunes, and $62^{+35}_{-37}\%$ of stars host earths. These estimates are still fairly rough but will be improved in the next few years.

2.6.6 Brown dwarfs

Microlensing planet searches have also yielded several important brown-dwarf discoveries. This includes the first isolated-brown-dwarf mass measurement (Gould et al. 2009) and the first two mass measurements of low-mass brown-dwarf binaries in the field (Choi et al. 2013). In particular, the latter demonstrates that the brown-dwarf binding-energy floor, previously found at larger separations, in fact holds at close separations as well. This is in sharp contrast to stars, for which the binding energies can be an order of magnitude smaller. Hence, it is likely that stars and brown dwarfs, at least those found in binaries, form by different mechanisms.

2.7. Future of microlensing planet searches

2.7.1 Second-generation surveys

For 15 years, from 1995 to 2010, microlensing planet searches took place within the context of the survey+follow-up strategy originally proposed by Gould and Loeb (1992). While one planet was found by blind operation of the surveys without any human intervention (Bennett et al. 2008), the great majority combined survey and follow-up data, occasionally from the surveys themselves (e.g. Bond et al. 2004). However, since 2010 there has been high-cadence ($> \text{hr}^{-1}$) coverage of about 10 square degrees by both the

OGLE (Udalski et al. 2005) and MOA (Bond et al. 2004) collaborations (operating from Chile and New Zealand respectively) and of a slightly smaller area by the Wise Survey (Shvartzvald & Maoz 2012) from Israel. This development is leading to a revolution in microlensing planet searches.

Previously only a relative handful of microlensing events were continuously monitored, which of course were those judged to be most favourable to finding planets. Hence, the majority of planets in this era were found in high-magnification events, even though intrinsically there are many more perturbations due to planetary caustics at low-to-moderate magnification. Thus, many more planets can be found with today's more intensive, near-continuous surveys.

However, just as important, these second generation surveys have a pre-determined observing strategy, so the detections and non-detections can be analysed on a rigorous statistical basis. This will enable much deeper understanding of the implications of microlensing detections, not only of planets but of binaries in which either one or both components is a brown dwarf. About a dozen survey-only planets have been discovered so far, mostly in the 2012 season (at the time of writing the 2010 season had not yet been systematically analysed).

In the near future the Korea Microlensing Telescope Network will inaugurate observations at three sites, Chile, South Africa, and Australia, using 1.6 m telescopes with 4 deg² cameras. Present plans call for a 10-minute cadence. This will greatly increase the planet detection rate.

2.7.2 Future of follow-up observations

Does the coming of second generation surveys spell the end of follow-up observations? Probably not. First, high-magnification events yield several types of information not readily obtained from the more common planet detections in low-magnification events, and these require more intensive observations for full exploitation.

OGLE-2012-BLG-0026 provides a striking illustration of several key points. First, this event took place in a northern bulge field, well outside the area monitored by multiple surveys. Second, even if it had been in a multi-survey field, it would have been covered only a few hours per night from each site, because the target was only 5 hours from the Sun when the event peaked. Third, this event was extremely important because it contained only the second two-planet system beyond the snow line. High-magnification events are much more sensitive to multi-planet detections than low-mag events (Gaudi, Nabor and Sackett 1998). These planets were detected only because a network of (mainly amateur) astronomers followed up the OGLE alert with intensive, round-the-globe observations.

MOA-2011-BLG-293 provides another important example. This high-mag event was in the combined survey area and was monitored by all three surveys on the night of the peak. However, since it was high-magnification, it was also alerted by μ FUN. With the follow-up data, Yee et al. (2012) were easily able to characterize the event. However, they also investigated whether the planet would have been considered detectable if there had been only survey data. Despite the $\Delta\chi^2 = 500$ improvement from a planetary fit, they were not convinced such a detection would have been claimed. Yee et al. (2013) concluded that no planet could be claimed for MOA-2010-BLG-311, despite a $\Delta\chi^2 = 140$ improvement. They argued that high-magnification events intrinsically require greater χ^2 improvement because the planetary perturbations are at the peak of the event. Thus, full exploitation of high-magnification events will likely require follow-up.

Finally, Gould and Yee (2013) showed that even the two isolated-star mass measurements made to date using 'terrestrial parallax' is an unexpectedly high number given

current observational protocol. They argued that one should expect only one per century(!). Such measurements are highly prized because they are the *only* way to measure the masses of low-mass, isolated, dark objects, such as free-floating planets and brown dwarfs. Indeed, one of the two measured objects was a brown dwarf from the thick disc (Gould et al. 2009). Gould and Yee (2013) proposed several different schemes for more aggressive follow-up that could potentially increase the rate of such measurements by a factor 100.

2.7.3 M31 planets

An M31 planet survey would open up a new frontier. At present, it is just assumed that planet frequencies will be the same in other galaxies, but the same could be said for metallicity distributions, dwarf-spheroidal populations, etc. Until we actually search for planets in other galaxies, our views on this question are no more than prejudice and guesswork. In addition, our line of sight towards the M31 bulge is not through the M31 disc, in strong contrast to the situation for the Milky Way. This would allow easy distinction between planet frequencies in its disc and bulge.

Microlensing is the only foreseeable method to search for M31 planets. Chung et al. (2006) showed that continuous monitoring of M31 with 2 m class telescopes could detect super-jupiters, primarily from giant-star sources in high-magnification events. They also argued that follow-up observations, triggered by high-magnification events and using 8 m class telescopes, could both greatly increase the rate of detection of these super-Jupiters and bring the mass threshold down as well.

S. Calchi Novati and I have been working on a different approach: continuous observations with the Large Binocular Telescope's Large Binocular Camera (LBT LBC). Our calculations show that we would be sensitive to high-magnification events with main-sequence sources. This would permit detection of lower-mass planets (because the planetary Einstein radius of these planets is comparable to the disc of a main-sequence star). One of the greatest difficulties of high-magnification events in M31 is that one generally is not able to fit for t_E , only $t_{\text{eff}} = u_0 t_E$ (Gould 1996). Without knowledge of t_E it would be very difficult to even determine the mass ratio q , since this $q t_E$ is an invariant of high-magnification microlensing models (Yee et al. 2012). However, since LBC can obtain simultaneous observations in V and R , the source colour would be measured, allowing an estimate of the source brightness from 'main-sequence fitting'. We have already obtained some LBT LBC observations that should enable us to determine if this approach is feasible.

2.7.4 Space missions

As first argued by Bennett and Rhie (1996), microlensing planet searches can be carried out much more effectively from space. The original driver was better photometry due to smaller and more stable seeing. In the Galactic bulge, most stars are blended with a sea of other stars, but space-based images can resolve these out. However, subsequently it was realized that space had another advantage: the possibility of infrared (IR) imaging. The microlensing fields that are currently being observed from the ground are fairly heavily obscured by dust, and even these would be greatly improved by IR imaging, which is much less affected by dust. But if one had an IR imager, one would actually target even denser star fields closer to the Galactic plane, which are even more heavily obscured. Several detailed proposals for such a 'Microlensing Planet Finder' were submitted to NASA by D. P. Bennett and collaborators but without success.

In the meantime, however, considerable enthusiasm developed in both the USA and Europe to put a wide-field IR imager in space to pursue dark energy studies. This created the possibility of a joint mission to pursue both dark energy and planetary microlensing. In fact, as part of the community discussion leading up to the 2010 ‘Decadal Report’ on future directions of American astronomy, I submitted a white paper entitled ‘Wide Field Imager in Space for Dark Energy and Planets’ (Gould 2009).

The current situation is encouraging but not secure. The European version of these proposals has been accepted by ESA and the resulting *Euclid* satellite is currently scheduled for launch in 2020. Unfortunately, microlensing planet searches are not part of its formal mission, but for several months each year, the satellite will only be able to look near the Galactic plane (where dark energy work is sub-optimal), so planet searches would be a good use of this time.

On the US side, the 2010 Decadal Survey ‘New Worlds, New Horizons’ adopted a *Wide-Field Infrared Space Telescope* (*WFIRST*) as its highest priority, with microlensing planet searches specified as one of its three main goals. Unfortunately, the US budget situation is such that even ‘highest priority’ does not guarantee timely launch.

If either *WFIRST* or *Euclid* does carry out significant microlensing studies, the scientific impact will be immense. Everything that I have described in this chapter and more will be carried out about ten times better. Planets down to Mars mass will be detectable beyond the snow line, the free-floating planet population will be probed down to Earth-mass objects, and masses would be available for a large fraction of the planets detected. The non-planetary microlensing events (automatically acquired as part of the observations) would probe brown dwarfs, low-mass binaries, and the stellar mass function deep in the Galactic bulge, where it has never been studied. Thus, microlensing planet searches continue to have great potential.

Acknowledgements

I thank the Instituto de Astrofísica de Canarias for the opportunity to deliver my lectures and their outstanding hospitality and support during my visit. I thank Jennifer C. Yee for a careful review of the manuscript. This work was supported in part by NSF grant 1103471.

REFERENCES

- Albrow, M. D. et al. 2000, *ApJ*, **534**, 894
- An, J. H. 2005, *MNRAS*, **356**, 1409
- An, J. H. & Gould, A. 2001, *ApJ*, **563**, L111
- Batista, V. et al. 2011, *A&A*, **511**, A102
- Beaulieu, J.-P. et al. 2006, *Nature*, **439**, 437
- Bennett, D. P. 2010, *ApJ*, **716**, 1408
- Bennett, D. P. & Rhie, S.-H. 1996, *ApJ*, **472**, 660
- Bennett, D. P. et al. 2008, *ApJ*, **684**, 663
- Bennett, D. P. et al. 2010, *ApJ*, **713**, 837
- Bond, I. A. et al. 2004, *ApJ*, **606**, L155
- Boss, A. P. 2006, *ApJ*, **643**, 501
- Bozza, V. 2010, *MNRAS*, **408**, 2188
- Cassan, A. et al. 2012, *Nature*, **481**, 167
- Choi, J.-Y. et al. 2013, *ApJ*, **768**, 129

- Chung, S.-J. et al. 2006, *ApJ*, **650**, 432
- Cumming, A. et al. 2008, *PASP*, **120**, 531
- Dominik, M. 1999, *A&A*, **349**, 108
- Dong, S. et al. 2006, *ApJ*, **642**, 842
- Dong, S. et al. 2007, *ApJ*, **664**, 862
- Dong, S. et al. 2009, *ApJ*, **695**, 970
- Einstein, A. 1936, *Science*, **84**, 506
- Gaudi, B. S., Nabor, R. M. & Sackett, P. D. 1998, *ApJ*, **502**, L33
- Gaudi, B. S. et al. 2008, *Science*, **319**, 927
- Gould, A. 1992, *ApJ*, **392**, 442
- Gould, A. 1994, *ApJ*, **421**, L71
- Gould, A. 1996, *ApJ*, **470**, 201
- Gould, A. 2000, *ApJ*, **542**, 785
- Gould, A. 2004, *ApJ*, **606**, 319
- Gould, A. 2008, *ApJ*, **681**, 2008
- Gould, A. 2009, Astro2010: The Astronomy and Astrophysics Decadal Survey, Science White Papers, no. 100, arXiv:0902.2211
- Gould, A. & Andronov, N. 1999, *ApJ*, **516**, 236
- Gould, A. & Gaucherel, C. 1997, *ApJ*, **477**, 580
- Gould, A. & Loeb, A. 1992, *ApJ*, **396**, 104
- Gould, A. & Yee, J. C. 2013, *ApJ*, **764**, 107
- Gould, A. et al. 2006, *ApJ*, **644**, L37
- Gould, A. et al. 2009, *ApJ*, **698**, 147
- Gould, A. et al. 2010, *ApJ*, **720**, 1073
- Gould, A., Shin, I.-G., Han, C., Udalski A. & Yee, J. C. 2013, *ApJ*, **768**, 126
- Griest, K. & Safizadeh, N. 1998, *ApJ*, **500**, 37
- Han, C. 2006, *ApJ*, **638**, 1080
- Han, C. et al. 2013, *ApJ*, **762**, L28
- Ida, S. & Lin, D. N. C. 2005, *ApJ*, **626**, 1045
- Laughlin, G., Bodenheimer, P. & Adams, F. C. 2004, *ApJ*, **612**, L73
- Liebes, S. 1964, *Phys. Rev.*, **133**, B835
- Mao, S. & Paczyński, B. 1991, *ApJ*, **374**, L37
- Mao, S. & Paczyński, B. 1996, *ApJ*, **473**, 57
- Muraki, Y. et al. 2011, *ApJ*, **741**, 22
- Paczynski, B. 1986, *ApJ*, **304**, 1
- Park, B. G. et al. 2004, *ApJ*, **609**, 166
- Pejcha, O. & Heyrovský, D. 2009, *ApJ*, **690**, 1772
- Poindexter, S. et al. 2005, *ApJ*, **633**, 914
- Refsdal, S. 1964, *MNRAS*, **128**, 259
- Refsdal, S. 1966, *MNRAS*, **134**, 315
- Renn, J., Sauer, T. & Stachel J. 1997, *Science*, **275**, 84
- Shvartzvald, Y. & Maoz, D. 2012, *MNRAS*, **419**, 3631
- Skowron, J. & Gould, A. 2012, *Acta Astron.*, submitted, arXiv:1203.1034
- Skowron, J. et al. 2011, *ApJ*, **738**, 87
- Shin, I.-G. et al. 2011, *ApJ*, **735**, 85
- Shin, I.-G. et al. 2012, *ApJ*, **755**, 2082

- Smith, M. C., Mao, S. & Paczyński, B. 2003, *MNRAS*, **339**, 925
- Sumi, T. et al. 2010, *ApJ*, **710**, 1641
- Sumi, T. et al. 2011, *Nature*, **473**, 349
- Udalski, A. et al. 2005, *ApJ*, **628**, L109
- Witt, H. 1990, *A&A*, **236**, 311
- Yee, J. C. et al. 2010, *ApJ*, **703**, 2082
- Yee, J. C. et al. 2012, *ApJ*, **755**, 102
- Yee, J. C. et al. 2013, *ApJ*, **769**, 77
- Yoo, J. C. et al. 2004, *ApJ*, **603**, 139